Monthly Notices of the ROYAL ASTRONOMICAL SOCIETY
MNRAS **505,** 1827–1840 (2021) https://doi.org/10.1093/mnras/stab1253
Advance Access publication 2021 May 12

# Planet Hunters TESS III: two transiting planets around the bright G dwarf HD 152843

N. L. Eisner [1]*, B. A. Nicholson,[1,2] O. Barragán [1], S. Aigrain,[1] C. Lintott [1], L. Kaye,[1] B. Klein [1], G. Miller,[1] J. Taylor [1], N. Zicher,[1] L. A. Buchhave [3], D. A. Caldwell,[4] J. Horner,[2] J. Llama,[5] A. Mortier [6,7], V. M. Rajpaul [6], K. Stassun [8], A. Sporer,[9] A. Tkachenko,[10] J. M. Jenkins,[11] D. Latham,[12] G. Ricker,[9] S. Seager,[9,13,14] J. Winn,[15] S. Alhassan,[16] E. M. L. Baeten,[16] S. J. Bean,[16] D. M. Bundy,[16] V. Efremov,[16] R. Ferstenou,[16] B. L. Goodwin,[16] M. Hof,[16] T. Hoffman,[16] A. Hubert,[16] L. Lau [16], S. Lee,[16] D. Maetschke,[16] K. Peltsch,[16,17] C. Rubio-Alfaro[16] and G. M. Wilson[16]

[1]*Department of Physics, University of Oxford, Keble Road, Oxford OX1 3RH, UK*
[2]*Centre for Astrophysics, University of Southern Queensland, Toowoomba, Queensland 4350, Australia*
[3]*DTU Space, National Space Institute, Technical University of Denmark, Elektrovej 328, DK-2800 Kgs. Lyngby, Denmark*
[4]*SETI Institute, 189 Bernardo Ave, Suite 200 Mountain View, CA 94043, USA*
[5]*Lowell Observatory, 1400 W. Mars Hill Rd., Flagstaff, AZ 86001, USA*
[6]*Astrophysics Group, Cavendish Laboratory, University of Cambridge, J.J. Thomson Avenue, Cambridge CB3 0HE, UK*
[7]*Kavli Institute for Cosmology, University of Cambridge, Madingley Road, Cambridge CB3 0HA, UK*
[8]*Department of Physics and Astronomy, Vanderbilt University, Nashville, TN 37235, USA*
[9]*Department of Physics and Kavli Institute for Astrophysics and Space Research, Massachusetts Institute of Technology, Cambridge, MA 02139, USA*
[10]*Institute of Astronomy, KU Leuven, Celestijnenlaan 200D, B-3001 Leuven, Belgium*
[11]*NASA Ames Research Center, Moffett Field, CA 94035, USA*
[12]*Harvard–Smithsonian Center for Astrophysics, 60 Garden St, Cambridge, MA 02138, USA*
[13]*Department of Earth, Atmospheric and Planetary Sciences, Massachusetts Institute of Technology, Cambridge, MA 02139, USA*
[14]*Department of Aeronautics and Astronautics, MIT, 77 Massachusetts Avenue, Cambridge, MA 02139, USA*
[15]*Department of Astrophysical Sciences, Princeton University, 4 Ivy Lane, Princeton, NJ 08544, USA*
[16]*Citizen Scientist, Zooniverse c/o University of Oxford, Keble Road, Oxford OX1 3RH, UK*
[17]*School of Computer Science & Technology, Algoma University, Sault Ste. Marie, ON P6A 2G4, Canada*

Accepted 2021 April 20. Received 2021 April 20; in original form 2021 March 13

## ABSTRACT

We report on the discovery and validation of a two-planet system around a bright ($V = 8.85$ mag) early G dwarf (1.43 $R_0$, 1.15 $M_0$, TOI 2319) using data from NASA's *Transiting Exoplanet Survey Satellite* (*TESS*). Three transit events from two planets were detected by citizen scientists in the month-long *TESS* light curve (sector 25), as part of the Planet Hunters TESS project. Modelling of the transits yields an orbital period of $11.6264^{+0.0022}_{-0.0025}$ d and radius of $3.41^{+0.14}_{-0.12}$ $R_\oplus$ for the inner planet, and a period in the range 19.26–35 d and a radius of $5.83^{+0.14}_{-0.14}$ $R_\oplus$ for the outer planet, which was only seen to transit once. Each signal was independently statistically validated, taking into consideration the *TESS* light curve as well as the ground-based spectroscopic follow-up observations. Radial velocities from HARPS-N and EXPRES yield a tentative detection of planet b, whose mass we estimate to be $11.56^{+6.58}_{-6.14}$ $M_\oplus$, and allow us to place an upper limit of 27.5 $M_\oplus$ (99 per cent confidence) on the mass of planet c. Due to the brightness of the host star and the strong likelihood of an extended H/He atmosphere on both planets, this system offers excellent prospects for atmospheric characterization and comparative planetology.

**Key words:** methods: statistical – planets and satellites: detection – stars: fundamental parameters – stars: individual: TIC 349488688, HD 152843.

## 1 INTRODUCTION

Systems with multiple transiting planets offer a wealth of information for exoplanetary science. In particular, they allow for comparative planetology: studying planets that have formed out of the same material, but have formed and evolved in different environments, receiving different amounts of incident flux from the host star, resulting in differing masses, radii and composition. Well characterized multiplanet systems therefore provide important model constraints that single-planet systems cannot, providing insight into planetary system architecture and evolutionary pathways, as well as informing ongoing planet population studies (e.g. Tremaine & Dong 2012; Dietrich & Apai 2020).

The *Kepler* mission (Borucki et al. 2010) revealed that multiplanetary systems are common (Latham et al. 2011), with almost half of all *Kepler* planets listed in the NASA Exoplanet Archive belonging to multiplanet systems (Akeson et al. 2013). However, the majority

* E-mail: nora.eisner@new.ox.ac.uk

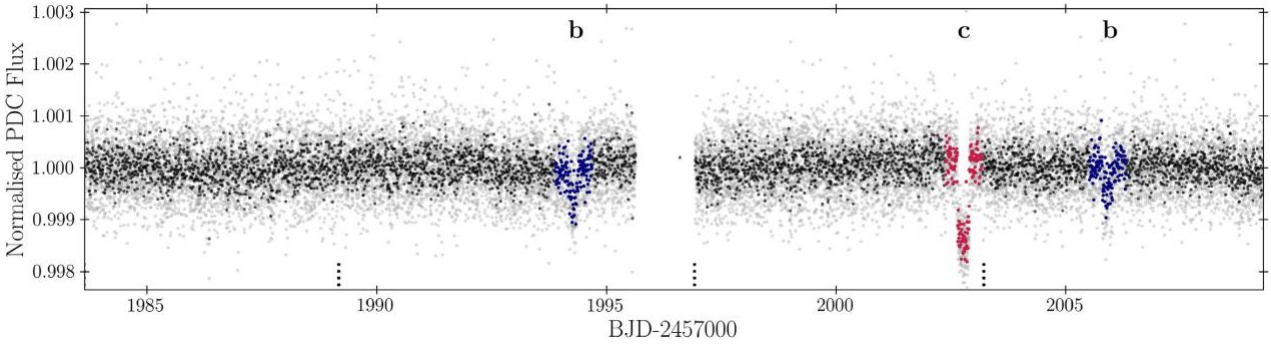


**Figure 1.** Flux time series for HD 152843 versus *TESS* Julian day (BJD-2457000.0) for Sectors 25. The light grey points show the short cadence data with a 2 min sampling, while the black points are 10 min averages. The dashed vertical lines at the bottom of the figure show the times of the *TESS* momentum dumps. The transit events are shown in blue and pink, corresponding to the inner and outer planet candidates.

of the hundreds of multiplanet systems found by *Kepler* are too faint to follow-up with ground-based high-resolution spectroscopy.This has resulted in most known multiplanet systems lacking well-determined masses, densities, bulk compositions, and atmospheric characterization, all of which are key to helping us understand the overall planet population.

NASA's *Transiting Exoplanet Survey Satellite* (*TESS*; Ricker et al. 2015), however, targets stars that are on average a 30–100 times brighter than those observed by the *Kepler* mission, thus allowing us to follow-up and constrain the properties of systems that were previously inaccessible. *TESS* has already discovered tens of previously unknown, multiplanet systems (e.g. Dragomir et al. 2019; Gandolfi et al. 2019; Quinn et al. 2019; Carleo et al. 2020; Fridlund et al. 2020; Gilbert et al. 2020; Mann et al. 2020; Leleu et al. 2021).

Detecting transiting multiplanet systems with longer-period planets is challenging due to the reduced transit probability of those planets, as well as the challenges associated with detecting planets showing single transits using automated detection algorithms. For this reason, alternative methods are often used to identify longer-period, single transit candidates, such as machine learning (e.g. Pearson, Palafox & Griffith 2018; Zucker & Giryes 2018), or visual vetting with the help of citizen science (Fischer et al. 2012; Eisner et al. 2021).

Furthermore, verifying the planetary nature of single transit objects is challenging, as the lack of a known orbital period complicates follow-up efforts. However, this is made easier in the situation of multiplanet systems. Latham et al. (2011) and Lissauer et al. (2012) independently showed that systems with multiple planet candidates are statistically less likely to be false positives, compared to single-planet systems. This is helpful to consider in following up single-transit, longer-period planets with closer companions

which are themselves more easily verifiable as true planetary companions.

Despite the large number of exoplanet discoveries made by *TESS* and *Kepler*, systems with more than one transiting planet around stars brighter than $V \backsim 10$ (the typical magnitude required for atmospheric follow-up, e.g. Fortenbach & Dressing 2020) containing planets with measured masses remain exceedingly rare. As of 2021 April, there are only 17 transiting planets (in 12 systems) with mass measurements better than 50 per cent precision around stars with $V < 10$ listed in the NASA Exoplanet Archive (Akeson et al. 2013). A list of these systems and their corresponding parameters can be found in Appendix A. Significant observing resources have been, and continue to be, devoted to each of them.

In this paper, we present a new multiplanet system, with the discovery of two planets orbiting around HD 152843. These candidates were initially identified in *TESS* Sector 25 by citizen scientists taking part in the Planet Hunters TESS (PHT) project (Eisner et al. 2021). In Section 2, we outline the discovery of the candidates and the vetting tests carried out based on the *TESS* photometric light curve. In Section 3, we discuss the spectroscopic data obtained with HARPS-N and EXPRES and in Section 4 we discuss the joint photometric and spectroscopic data analysis. Finally, the results are discussed in Section 5 and the conclusions presented in Section 6.

## 2 TESS PHOTOMETRY

HD 152843 was observed by *TESS* only in Sector 25 of the primary mission. The spacecraft obtained images at a cadence of 2-s, which were combined onboard into 2-min cadence data products. These were processed and reduced by the Science Processing Operations Center (SPOC; Jenkins et al. 2016). Throughout this work, we use the pre-search data conditioning (PDC) light curve from the SPOC pipeline, as shown in Fig. 1. The data gap seen in the centre of the full light curve corresponds to the time taken ($\backsim$ 1 d) for the spacecraft to send the data to Earth and re-orient itself. The black dashed lines at the bottom of the figure indicate the times of the periodic momentum dumps caused by the firing of the thrusters as the spacecraft adjusts the spin rate of the reaction wheels approximately every 5.5 d.

### 2.1 Discovery of HD 152843 b and HD 152843 c

The light curve shown in Fig. 1 exhibits three transit events belonging to different transiting planets, with HD 152843 b shown in blue and HD 152843 c shown in pink. The first transit event of HD 152843 b

($T_{\mathrm{BJD-2457000}} \backsim$1994.28 d) and the single transit event of HD 152843 c

($T_{\mathrm{BJD-2457000}}$ 2002.77 d) were flagged as a single Threshold Cross-ing Event (TCE) by the SPOC pipeline, as two events caused bythe same 'object'. However, due to the different depths of these two transits, the TCE was not promoted to TESS Object of Interest (TOI) status, due to the assumption that the two events correspond to the primary and secondary eclipses of an eclipsing binary. The second transit event of HD 152843 b was not flagged by the pipeline.

All three transit events were identified by the PHT citizen science project (Eisner et al. 2021). PHT, which is hosted by the Zooniverse platform (Lintott et al. 2008, 2011), harnesses the power of over 25 000 registered citizen scientists who visually vet all of the *TESS* two-min cadence light curves in search for transit events that were ignored

or missed by the main transit detection pipeline and other teams of professional astronomers. The light curve of HD 152843 was seen by 15 citizen scientists, 12 of whom identified all three transit events, and 3 who identified only two out of the three events. The target was initially brought to the attention of the PHT research team via the PHT discussion forum.[1] We uploaded both planet candidatesto the Exoplanet Follow-up Observing Program for TESS (ExoFOP-TESS) site on 2020 August 7 as a community TESS Object of Interest (cTOI). The inner planet has since been promoted to the priority 1 (1 = highest priority, 5 = lowest priority) candidate TOI 2319.01.

### 2.2 Excluding false positive scenarios

Astrophysical and instrumental false positives are common in the *TESS* data, in particular due to the large (21 arcsec pix$^{-1}$) pixel scale. We used the publicly available Lightcurve Analysis Tool for Transiting Exoplanets (LATTE; Eisner, Lintott & Aigrain 2020a) in order to perform standard diagnostic tests that help to rule out false positive scenarios including background eclipsing binaries, systematic effects, and background events such as asteroids passing through the field of view. For a full description of the diagnostic tests, we refer the reader to Eisner et al. (2020a), however, in brief the tests include:

(i) Checking that the transit events do not coincide with the times of the periodic momentum dumps.
(ii) Checking that the $x$ and $y$ centroid positions are smoothly varying with time in the vicinity of the transit events.
(iii) Examining light curves of the five nearest two-min cadence *TESS* stars to check for systematic effects.
(iv) Examining light curves extracted for each pixel surrounding the target in order to ensure that the signal is not the result of a background eclipsing binary, a background event or caused by systematics.
(v) Checking that there are no spurious signals, such as sudden jumps or strong variations, in the background flux.
(vi) Comparing transit shapes and depths when extracted with different aperture sizes.
(vii) Comparing between the average in-transit and average out-of-transit flux, as well as the difference between them.
(viii) Checking the location of nearby stars brighter than $V$-band magnitude 15 as queried from the *Gaia* Data Release 2 catalogue (Gaia Collaboration 2018).
(ix) Performing the box-Least-Squares fit to search for additional signals.

Tests (i) to (iv) enabled us to rule out events caused by systematic effects due to the satellite or instrument, and tests (iii) to (viii) increased our confidence that the signals are not caused by astrophysical false positives, such as blends where the photometric aperture of a bright target contains a faint eclipsing binary.

As blends are common in the *TESS* data, we searched for nearby *Gaia* Data Release 2 catalogue stars (Gaia Collaboration 2018) within 110 arcsec of the target, and found there to only be a single star with a $V$-band magnitude brighter than 15, as shown by the orange circle in Fig. 2, where the red star shows HD 152843 and the red outline highlights the aperture used to extract the light curve.

In order to rule out this nearby star as the cause of the transit events, we calculated the magnitude difference between HD 152843 and the faintest companion star that could plausibly be responsible for the observed transit shapes and depths. Following the methodology outlined by Vanderburg et al. (2019) and the transit parameters derived using `pyaneti` (see Section 4.4), we show that the maximum magnitude difference between the target star and a possible background contaminant is 1.5 magnitude in the $V$ band. This allows us to confidently conclude that the 14.4 magnitude star (5.6 magnitude fainter than HD 152843), located at an angular separation of 31.3 arcsec, is not responsible for either of the planetary signals.

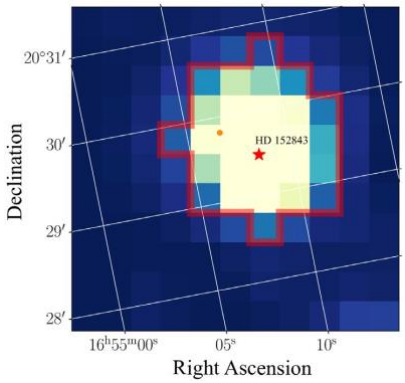


**Figure 2.** The median *TESS* image around HD 152843. The aperture used to extract the light curve is shown by the red outline and the orange dot depicts the location of the only star brighter than $V$ 15 within 110 arcsec of the target (red star), as queried by *Gaia* DR2 (Gaia Collaboration 2018). This nearby star ($V$ = 14.4) is located at an angular separation of ∼ 31.3 arcsec.

### 2.3 Limits on additional planets

We quantify the detectability of additional planets in the *TESS* light curve using a transit injection and recovery test (e.g. Eisner et al. 2020b). In brief, we removed the known transit events prior to injecting synthetic signals into the PDC *TESS* light curve. The injected signals were generated using the BATMAN package (Kreidberg 2015), with planet radii ranging from 1 to 12 $R_\oplus$ and periods ranging from 3 to 24 d, both sampled at random from a log-uniform distribution. The impact parameter and eccentricity were assumed to be zero throughout and we used a quadratic limb-darkening law with $q1$ and $q2$ of 0.16 and 0.59, respectively, as taken from table 15 in Claret (2017) using the stellar parameters given in Table 1. Once the signals were injected, we used an iterative non-linear filter (Aigrain & Irwin 2004) to estimate and subtract residual systematics on time-scales > 1.7 d.

We simulated and injected a total of 750 000 transit events. The Box Least Squares (BLS; Kovács, Zucker & Mazeh 2002) algorithm was then used to try to recover the injected signals. The BLS search sampled a frequency grid that was evenly-spaced from 0.01 to 1 d$^{-1}$. For each simulation, we recorded the period and orbital phase corresponding to the highest peak in the BLS periodogram. If the recovered orbital period and phase agreed to within 1 per cent of the injected period, the signal was deemed to be correctly identified. The completeness, assessed in radius and period bins with width of 0.25 $R_\oplus$ and 0.75 d, respectively, was then taken to be the fraction of correctly identified transit signals.

The results, shown in Fig. 3, highlight, as expected, that the automated BLS search is strongly biased towards detecting shorter period planets that transit multiple times in the light curve. The limited duration of the *TESS* observations of ∼ 27 d, interrupted

[1] https://www.zooniverse.org/projects/nora-dot-eisner/planet-hunters-tess/talk/2112/1552434?comment = 2520798

**Table 1.** Stellar parameters.

| Parameter | Value | Source |
|---|---|---|
| **Identifiers** | | |
| HD | 152843 | |
| TOI | 2319 | |
| TIC | 349488688 | Stassun et al. (2019) |
| *Gaia* DR2 | 4564566554995619072 | *Gaia* eDR3[a] |
| 2MASS | J16550834 + 2029287 | 2MASS[b] |
| **Astrometry** | | |
| $\alpha_{J2000}$ | 16:55:08.373 | *Gaia* eDR3[a] |
| $\delta_{J2000}$ | 20:29:29.509 | *Gaia* eDR3[a] |
| Distance (pc) | 107.898 ± 0.317 | Bailer-Jones et al. (2018) |
| $\pi$ (mas) | 9.161 ± 0.015 | *Gaia* eDR3[a] |
| **Photometry** | | |
| B | 9.380 ± 0.020 | *Tycho-2*[c] |
| V | 8.850 ± 0.010 | *Tycho-2*[c] |
| J | 7.896 ± 0.018 | 2MASS[b] |
| H | 7.655 ± 0.016 | 2MASS[b] |
| K | 7.629 ± 0.020 | 2MASS[b] |
| W1 | 7.563 ± 0.031 | WISE[a] |
| W2 | 7.594 ± 0.020 | WISE[d] |
| W3 | 7.607 ± 0.019 | WISE[d] |
| **Physical Properties** | | |
| Spectral Type | G0 | |
| Effective Temperature $T_{eff}$ (K) | 6310 ± 100 | This work |
| Surface gravity log $g_*$ (cgs) | 4.19 ± 0.03 | This work |
| $v$ sin $i_*$(km s$^{-1}$) | 8.38 ± 0.50 | This work |
| [M/H] (dex) | −0.22 ± 0.08 | This work |
| [Fe/H] (dex) | −0.16 ± 0.05 | This work |
| $v_{mic}$ (km s$^{-1}$) | 1.66 ± 0.13 | This work |
| $v_{mac}$ (km s$^{-1}$) | 2 | Bruntt et al. (2010) |
| Stellar mass $M_*$ ($M_0$) | 1.15 ± 0.04 | This work |
| Stellar radius $R_*$ ($R_0$) | 1.43 ± 0.02 | This work |
| Stellar density $\rho_*$ ($\rho_0$) | 0.40 ± 0.03 | This work |
| Star age (Gyr) | 3.97 ± 0.75 | This work |

[a]*Gaia* early Data Release 3 (eDR3; Gaia Collaboration 2021). [b]Two-micron All Sky Survey (2MASS; Cutri et al. 2003). [c]*Tycho*-2 catalogue (Høg et al. 2000). [d]Wide-field Infrared Survey Explorer catalogue (WISE; Cutri & et al. 2013).

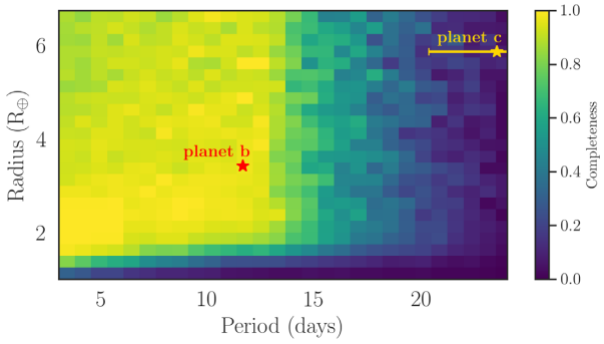


**Figure 3.** The recovery completeness of injected transit signals into the light curve of HD 152843 as a function of the radius and orbital period. The signals were recovered using a BLS search. The properties of HD 152843 band HD 152843 c are shown by the red and yellow star, respectively.

by a 1.3 d data gap, results in a sharp decline in completeness for periods longer than around 13 d. For planets greater than 2 $R_\oplus$, we recover 94 per cent of signals with periods between 12 and 13 d and 78 per cent of signals with periods between 14 and 15 d. The completeness for the parameters of planet b is close to 100 per cent, while the completeness for the parameters of planet c is close to 0 per cent due to the fact that there is only one transit within the available *TESS* light curve. We caution that the simulated signals were injected into the PDC light curve, which has already undergone detrending and systematics corrections by the SPOC pipeline. The presented recovery rates are therefore systematically higher than one might otherwise expect if the signals had been injected into the raw light curve (e.g. Lienhard et al. 2020). Overall, this analysis highlights the difficulties associated with detecting longer-period planets using automated algorithms, and demonstrates a need for alternative detection methods such as citizen science.

## 3 SPECTROSCOPIC DATA

### 3.1 Reconnaissance spectra

We made use of the Las Cumbres Observatory (LCO) telescopes with the Network of Robotic Echelle Spectrographs (NRES; Brown et al. 2013). This fibre-fed spectrograph, mounted on a 1.0-m telescope, has a resolution of R= 53 000 and a wavelength coverage of 380 to 860 nm. We obtained two spectra of HD 152843 on the 15 and 22 August 2020 with per pixel signal-to-noise ratios (SNR) of 38 and 25 at 520 nm, respectively. The two spectra gave radial velocity estimates of 9.7 ± 0.2 km s$^{-1}$ and 9.6 ± 0.7 km s$^{-1}$, which are

consistent within their uncertainties, and thus allowed us to rule out the possibility that the transit events are caused by an eclipsing binary.

### 3.2 High-resolution spectra

We acquired high-resolution (R ≈ 115 000) spectra with the High Accuracy Radial velocity Planet Searcher in the Northern hemisphere (HARPS-N; Cosentino et al. 2012, 2014) spectrograph mounted at the 3.6-m Telescopio Nazionale Galileo in La Palma, Spain, via Director's Discretionary Time (program ID A41DDT4). We obtained 18 spectra between 2020 September 5 and November 11 (mean SNR 89 at ∼550 nm). Each spectrum has simultaneous wavelength calibration with a Fabry–Perot etalon and was reduced via the standard HARPS Data Reduction Software (DRS; Baranne et al. 1996) using a G2 spectral template (mean RV uncertainty ∼4.2 m s$^{-1}$). Additionally, we extracted the HARPS-N radial velocity (RV) measurements using the TERRA pipeline (Anglada-Escude´ & Butler 2012), which uses a template-matching approach based on a template generated by stacking all of the spectra. The results extracted using DRS and TERRA have comparable uncertainties, with a slightly larger root-mean-square scatter in the TERRA extracted data. Around 71 per cent of the DRS/TERRA RVs agree within 1$\sigma$ and around 82 per cent agree within 2$\sigma$ . For the remainder of our analysis, we used the data extracted with the DRS.

We derived the $\log R^{\rm t}_{\rm HK}$ values for the HARPS-N spectra with SNR > 100 using the calibrations of Noyes et al. (1984), and found the values to range from −4.96 to −4.94 with a mean value of −4.95. This low value suggests that HD 152843 is a quiet star. We also note that there is no correlation between the $\log R^{\rm t}_{\rm HK}$ values and the radial velocities.

In addition to the HARPS-N observations, we obtained 22 spectra between 2020 September 9 and October 10 using the high-resolution ($R \approx 150\,000$) EXtreme PREcision Spectrometer (EXPRES; Jurgenson et al. 2016; Blackman et al. 2020; Petersburg et al. 2020) mounted on the 4.3-m Lowell Discovery Telescope (LDT; Levine et al. 2012), USA. Each spectrum was calibrated using a Thorium Argon lamp and a stabilized Laser Frequency Comb and the RVs were extracted using the EXPRES analysis pipeline (for detail, see Petersburg et al. 2020). Due to poor seeing and high airmass, 12 of those spectra (with SNR < 25 at 550 nm) were not used for further analysis. The mean SNR and mean RV uncertainty of the used spectra are 82 and 9.5 ∼ m s$^{-1}$, respectively. All HARPS-N and EXPRES RV measurements are listed in Table 2.

**Table 2.** Radial velocity measurements.

| Time (BJD-2457000) | RV (m s$^{-1}$) | $\sigma_{RV}$ (m s$^{-1}$) | SNR | Source |
|---|---|---|---|---|
| 2098.3521 | 4.2460 | 1.7400 | 155.1 | HARPS-N |
| 2101.6407 | −3.4170 | 12.1000 | 19.0 | EXPRES* |
| 2101.6553 | 19.1100 | 13.8290 | 16.0 | EXPRES* |
| 2101.6701 | −27.3050 | 14.6120 | 14.0 | EXPRES* |
| 2101.6849 | −26.5790 | 14.0830 | 14.0 | EXPRES* |
| 2102.3412 | − 4.4874 | 2.3570 | 117.5 | HARPS-N |
| 2102.6207 | 11.1370 | 11.9490 | 20.0 | EXPRES* |
| 2102.6351 | 10.9350 | 10.7270 | 21.0 | EXPRES* |
| 2102.6519 | 15.8470 | 12.4080 | 20.0 | EXPRES* |
| 2102.6656 | −0.8630 | 11.5030 | 23.0 | EXPRES* |
| 2102.6843 | 26.9160 | 11.7640 | 22.0 | EXPRES* |
| 2102.6999 | −24.1910 | 11.2430 | 22.0 | EXPRES* |
| 2102.7140 | −15.1840 | 12.8060 | 18.0 | EXPRES* |
| 2102.7312 | −43.8920 | 14.5010 | 13.0 | EXPRES* |
| 2104.3651 | −8.9263 | 18.0372 | 19.9 | HARPS-N* |
| 2110.3253 | − 3.5140 | 3.2192 | 86.6 | HARPS-N |
| 2111.3788 | 1.8856 | 2.7648 | 99.8 | HARPS-N |
| 2117.3242 | 5.3618 | 2.9210 | 95.2 | HARPS-N |
| 2119.3255 | 5.5608 | 3.2501 | 78.5 | HARPS-N |
| 2120.3307 | 0.2539 | 2.2039 | 126.2 | HARPS-N |
| 2120.4134 | 3.4885 | 3.3055 | 85.9 | HARPS-N |
| 2120.6143 | 5.4070 | 4.9410 | 95.0 | EXPRES |
| 2123.5929 | − 0.2250 | 5.3170 | 81.0 | EXPRES |
| 2123.6069 | 0.1490 | 4.9690 | 83.0 | EXPRES |
| 2125.3192 | − 1.6649 | 2.4766 | 110.9 | HARPS-N |
| 2126.3165 | − 6.6282 | 4.4202 | 64.7 | HARPS-N |
| 2126.5970 | − 1.0650 | 8.9100 | 41.0 | EXPRES |
| 2126.6118 | 11.0790 | 6.8700 | 57.0 | EXPRES |
| 2127.3185 | 4.9884 | 3.9503 | 71.8 | HARPS-N |
| 2128.3180 | 9.1121 | 3.1712 | 87.2 | HARPS-N |
| 2129.5838 | 5.0890 | 5.1920 | 92.0 | EXPRES |
| 2129.5967 | 13.1530 | 5.8300 | 64.0 | EXPRES |
| 2130.3156 | 1.4459 | 6.3500 | 45.3 | HARPS-N |
| 2130.5850 | 9.9870 | 5.1790 | 90.0 | EXPRES |
| 2132.5928 | 8.5890 | 4.4480 | 114.0 | EXPRES |
| 2132.6078 | 5.3240 | 4.8730 | 110.0 | EXPRES |
| 2152.2939 | 1.4524 | 2.5161 | 112.1 | HARPS-N |
| 2153.2902 | −4.2017 | 2.4502 | 115.7 | HARPS-N |
| 2154.2902 | 3.2138 | 3.6046 | 80.8 | HARPS-N |
| 2155.2908 | − 11.5868 | 7.1983 | 44.0 | HARPS-N |

*Indicates that the spectrum was not used for further analysis due to low signal to noise (SNR < 45). The SNRs are calculated at 550 nm.

## 4 DATA ANALYSIS

### 4.1 Stellar atmospheric parameters

The fundamental stellar parameters of HD 152843, namely the effective temperature ($T_{\rm eff}$), surface gravity ($\log g$), metallicity ([M/H]), projected rotational velocity ($v \sin i$), and microturbulent velocity ($\xi_t$), were extracted using three independent methods: ARES MOOG,[2] Grid Search in Stellar Parameters (GSSP),[3] and Stellar Parameter Classification (SPC).

The ARES+MOOG method derives stellar atmospheric parameters using a curve-of-growth method based on the equivalent widths (EWs) of the Fe I and Fe II lines (for details, see Sousa 2014). The EWs of the spectral lines were automatically extracted from a stacked spectrum of all of the HARPS-N data (with SNR > 45), using the ARES2 code (Sousa et al. 2015). The stacked spectrum has an SNR 350 at 6000 Å. The radiative transfer code MOOG (Sneden 1973) was then used to extract the stellar parameters, assuming local thermodynamic equilibrium (LTE) and using a grid of ATLAS plane-parallel model atmospheres (Kurucz 2013). The value of log g was subsequently further refined (Mortier et al. 2014) and systematic and precision errors combined in quadrature. The method yields the following values: $T_{\rm eff}$ 6348 ± 100 K, $\log g$ 4.31 ± 0.12, [Fe/H] = −0.16 ± 0.06, and $\xi_t$ = 1.82 ± 0.13 km s$^{-1}$.

We also used the open access GSSP code (Tkachenko 2015), which compares the normalized observed spectrum with a grid of synthetic spectra. A stacked spectrum of all of the HARPS-N data (with SNR > 45) was used for this analysis. The goodness of fit of each synthetic spectrum was assessed using a $\chi^2$ metric. The atmospheric models used as part of this code were pre-computed using the LLMODELS

[2]ARESv2: http://www.astro.up.pt/~sousasag/ares/; MOOG 2017: http://www.as.utexas.edu/~chris/moog.html

[3]GSSP: https://fys.kuleuven.be/ster/meetings/binary-2015/gssp-software-package

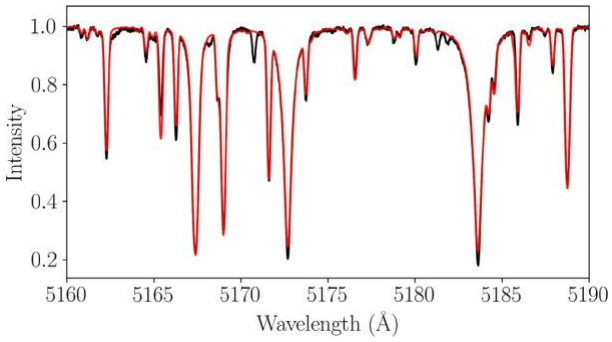


**Figure 4.** Section of the stacked HARPS-N spectra with SNR > 45 (black) and the best-fitting model as determined and computed with the GSSP software (red). The parameters and abundances of this best-fitting model, combined with the results from the ARES+MOOG and SPC analysis, were used to determine the stellar parameters listed in Table 1.

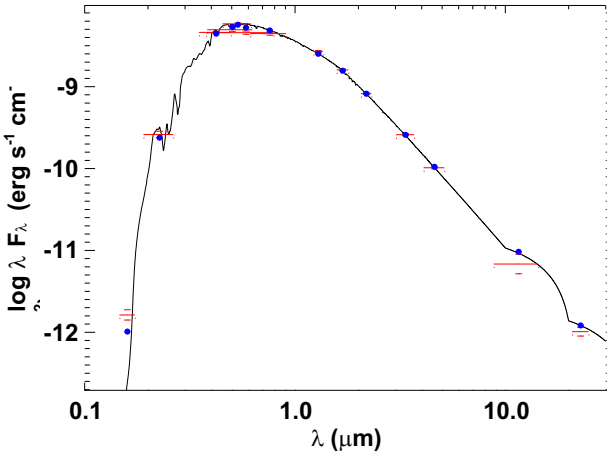


**Figure 5.** SED of HD 152843. Red symbols represent the observed photo- metric measurements, where the horizontal bars represent the effective width of the passband. Blue symbols are the model fluxes from the best-fitting Kurucz atmosphere model (black).

software (Shulyak et al. 2004) and the code assumed LTE. We independently optimized the abundances of Fe, Mg, Ti, Cr, and Ni. The best-fitting spectral model is shown in Fig. 4.

In order to determine the best-fitting parameters and abundances, the $\chi^2$ value was recorded for each combination of parameters. The projected $\chi^2$ values were then fit with a fourth-order polynomial for each parameter in order to determine the global minimum, which corresponds to the value of the best-fitting parameter. The uncertainties were taken as the intersection between the polynomial and the $1\sigma$ uncertainty limit. The following atmospheric parameters were obtained using GSSP: $T_{\rm eff} = 6368 \pm 100$ K, log g $= 4.16 \pm 0.10$, [M/H] $= -0.17 \pm 0.05$, [Fe/H] $= -0.16 \pm 0.05$, $v \sin i = 8.56 \pm 0.5$ km s$^{-1}$ and $\xi_t = 1.50 \pm 0.15$ km s$^{-1}$. We note that the derived $v \sin i$ value is not representative of the true rotational velocity of the star; instead, it represents a combined line broadening due to rotation and macroturbulence. Since we do not rely on the rotation rate of the star in our subsequent analysis, we find disentangling the effects of rotation and macroturbulent velocity to be beyond the scope of this study.

Finally, we used the SPC tool (for details, see Buchhave et al. 2012, 2014). Similarly to GSSP, SPC uses spectral synthesis, which was independently carried out on each HARPS-N spectrum (where SNR > 45). We obtained the following values: $T_{\rm eff} = 6175 \pm 50$ K, log g $= 4.15 \pm 0.10$, [M/H] $= -0.26 \pm 0.08$, and $v \sin i = 8.2 \pm 0.5$ km s$^{-1}$.

The values listed in Table 1, the averages of the results obtained from these three methods, were used for all subsequent analysis. Finally, we note that the spectra show almost no sign of Ca H and K re-emission, suggesting low magnetic activity.

### 4.2 SED fitting

As an independent determination of the basic stellar parameters, we performed an analysis of the broad-band spectral energy distribution (SED) of the star together with the *Gaia* DR2 parallax (adjusted by +0.08 mas to account for the systematic offset reported by Stassun & Torres 2018), in order to determine an empirical measurement of the stellar radius, following the procedures described in Stassun & Torres (2016), Stassun, Collins & Gaudi (2017), and Stassun et al. (2018).We pulled the $B_T V_T$ magnitudes from *Tycho-2*, the $JHK_S$ magnitudesfrom *2MASS*, the W1–W4 magnitudes from *WISE*, the $GG_{BP}G_{RP}$ magnitudes from *Gaia*, and the FUV and NUV magnitudes from *GALEX*. Together, the available photometry spans the full stellar SED over the wavelength range 0.15–22 $\mu$m (see Fig. 5).

We performed a fit using Kurucz stellar atmosphere models, with $T_{\rm eff}$, [Fe/H], and log $g$ adopted from the spectroscopic analysis. The remaining free parameter is the extinction $A_V$, which we limited to the maximum line-of-sight value from the Galactic dust maps of Schlegel, Finkbeiner & Davis (1998). The resulting fit (Fig. 5) has a reduced $\chi^2$ of 1.9; the reduced $\chi^2$ improves to 1.1 if we exclude the *GALEX* FUV flux, which exhibits a modest UV excess suggestive of chromospheric activity. We find a best-fitting $A_V = 0.04^{+0.05}_{-0.04}$.

Integrating the (unreddened) model SED gives the bolometric flux at Earth $F_{\rm bol} = 7.72 \pm 0.18 \times 10^{-9}$ erg s$^{-1}$ cm$^{-2}$. Taking the $F_{\rm bol}$ and $T_{\rm eff}$ together with the *Gaia* parallax gives the stellar radius, $R_* =$ 1.42 ± 0.05 R$_\odot$. In addition, we can estimate the stellar mass from the spectroscopic log $g$ together with $R_*$ from above, giving $M_* =$ 1.11 ± 0.15 M$_\odot$, which is consistent with that empirical relations of Torres, Andersen & Giménez (2010), giving $M_*$ 1.22 0.07 M$_\odot$. Finally, we can use the star's rotation and mild UV excess (Fig. 5) to estimate an age via empirical rotation–activity–age relations. The observed FUV excess implies a chromospheric activity of log $R^{\rm t}_{\rm HK}$ 4.51 0.05 via the empirical relations of Findeisen, Hillenbrand & Soderblom (2011), which in turn implies a stellar rotation period of $P_{\rm rot}$ 5.0 0.9 d via the empirical relations of Mamajek & Hillenbrand (2008), consistent with the upper limit $P_{\rm rot}/\sin i$ 8.7 d obtained from the spectroscopic $v \sin i$ and $R_*$.

### 4.3 Stellar mass, radius, age, and distance

The stellar parameters were extracted using isochrones and stellar evolutionary tracks. For this analysis, the combined ARES MOOG, GSSP and SPC effective temperature and metallicity were used as inputs, along with the Gaia eDR3 parallax, and the magnitude of the star in eight bands. All of the values used for this analysis are presented in Table 1.

For an in-depth discussion of this analysis, see Mortier et al. (2020), however, in brief, this analysis made use of the ISOCHRONES package (Morton 2015), using stellar models from the Dartmouth Stellar Evolution Database and from the MESA isochrones and Stellar Tracks (MIST; Choi et al. 2016). We used MULTINEST (Ferozet al. 2019) for the likelihood analysis and 400 live points. The

analysis was run six times: for each of the stellar models (Dartmouth/MIST) it was run three times using the $T_{\rm eff}$ and metallicity from the spectroscopic analysis (Section 4.1). The stellar values were extracted from the combined posteriors, taking the median and the 16th and 84th quantiles. The stellar mass, radius, density and age are listed in Table 1.

### 4.4 Joint transit and RV modelling

The transit and RV data were jointly analysed using the openaccess `pyaneti` code (Barragán, Gandolfi & Antoniciello 2019). In brief, `pyaneti` creates marginalized posterior distributions for different parameters by sampling the parameter space using a Markov chain Monte Carlo (MCMC) approach. We use the limb-darkened quadratic models by Mandel & Agol (2002) to fit the flattened transits. The RV data are fit with Keplerian RV models.

We first modelled the transits. Since planet c transits only once, the two planets were analysed independently. For planet b both transits were fitted simultaneously. This allowed us to fit for transitepoch, orbital period, impact factor, scaled planet radius, and scaled semimajor axis.

The single transit event (planet c) was modelled by fitting for the same parameters as for planet b, with the exception of the orbital period and scaled semimajor axis, as these cannot be constrained in the case of a single transit event. Instead, we obtained a possible period range of 13 to 35 d at the 99 per cent confidence interval, using the relations presented in Osborn et al. (2016) and assuming a circular orbit. These results were used to create uniform priors for all the transit model parameters, for a joint RV and transit analysis.

All fitted parameters and priors used for the joint modelling are presented in Table 3. We note that for this analysis, we allow the orbits to be eccentric in order to give more flexibility to the analysis. We sample for the stellar density $\rho_*$, and we recover the scaled semimajor axis for each planet in the system using Kepler's third law. We use a Gaussian prior on $\rho_*$ using the stellar mass and radius derived in Section 4.3. We also note that because planet c only exhibits a single-transit event we use a wide uniform prior on its period, based on the results from the single-transit analysis. However, we truncated the lower period limit at 19.26 d, as a shorter orbital period would have necessarily resulted in further transit events being present within the *TESS* light curve.

We sampled the parameter space using an MCMC approach with 500 independent chains and created posterior distributions using 5000 iterations of converged chains with a thin factor of 10. This generated a posterior distribution made with 250 000 independent samples for each parameter. The fitted parameters extracted from such posteriors can be found in Table 3. We note that the model and data only weakly constrain the orbital period of HD 152843 c, $P_c$. Furthermore, posterior distributions for the semi-amplitudes of both planets, $K_b$ and $K_c$, are truncated at zero. These posteriors and their correlations are shown in Fig. 6.

The posterior of $K_b$ corresponds to a $2\sigma$ detection, $3.09^{+1.76}_{-1.66}$ m s$^{-1}$, while planet c is not detected with an upper limit of 5.6 m s$^{-1}$, at 99 per cent confidence level. Figs 7 and 8 show the derived transit and RV models, respectively, together with the corresponding data.

### 4.5 Statistical validation

The open source python package `VESPA` was used to calculate the statistical false positive probability (FPP) of both the planet candidates (Morton 2012, 2015; Morton et al. 2016). In brief, `VESPA` computes the probabilities of a number of astrophysical scenarios that could result in the transit events using a Bayesian framework. These consist of HEB (hierarchical eclipsing binary), EB (eclipsing binary), and BEB (background eclipsing binary). A population of stars is simulated for each scenario using the `TRILEGAL` galactic model (Girardi et al. 2005) and the shape of the simulated transits compared to the transits in the observed *TESS* light curve. This results in a likelihood for each false positive scenario.

The FPPs for HD 152843 b and HD 152843 c are 0.05 per cent and <0.001 per cent, respectively, meaning that they are both below the traditionally required threshold of FPP < 1 per cent (Crossfield et al. 2016; Morton et al. 2016). We also note that the `VESPA` model does not consider multiplicity in planet systems, which has been shown to decrease the FPP by at least an order of magnitude (Lissauer et al. 2011, 2012, 2014). Lissauer et al. (2012), for example, estimated that systems with two or more planets in the *Kepler* data were 25 times less likely to be false positives. Furthermore, the derived upper mass limits of both planets enable us to rule out that the events are caused by an eclipsing binary. As both planet candidates reach the required threshold of 99 per cent confidence level, we consider both HD 152843 b and HD 152843 c statistically validated.

## 5 RESULTS AND DISCUSSION

The inner planet HD 152843 b ($P_{\rm b} = 11.6264^{+0.0022}_{-0.0025}$ d) has a radius of $R_{\rm b} = 3.41^{+0.14}_{-0.12}$ R$_\oplus$ while the outer planet HD 152843 c has a radius of $R_{\rm c} = 5.83^{+0.14}_{-0.14}$ R$_\oplus$. The radial velocity measurements allowed us to constrain the mass of the innermost planet to $M_{\rm b} = 11.56^{+6.58}_{-6.14}$ M$_\oplus$ and derive an upper mass limit of the outer planet (i.e. of planet c) of $M_{\rm c} < 27.5$ M$_\oplus$. Even though the obtained spectroscopic data do not provide a $3\sigma$ detection of the mass of either planet, the derived upper mass limits allow us to confirm that the transit signals seen in the *TESS* light curve are not the result of an eclipsing binary. Furthermore, they allow us to make predictions about future photometric and spectroscopic follow-up observations (see Sections 5.1 and 5.2).

While the orbital period of the inner planet is well determined, based on the two transit events seen in the *TESS* light curve, this is not the case for the singly transiting outer planet. We therefore constrain $P_{\rm c}$ based on the minimum period allowed by the *TESS* light curve, the transit duration and shape, and the joint modeling of the transit and RVs.

As shown in Fig. 6, the joint modelling of the light curve and the RVs produce a truncated posterior distribution for $P_{\rm c}$. This distribution favours orbital periods of around 23 d. While this could indicate a 2:1 mean motion resonance (MMR) with planet b, this could also be an artefact introduced into the modelling by planet b. Furthermore, while we can rule out orbital periods shorter than 19.26 d, it is possible that HD 152843 c has an orbital period of, or close to, 19.375 d, which would be a 5:3 MMR with HD 152843 b. The dynamical stability of these orbits and the effects of resonances in multiplanet systems are further discussed in Sections 5.3 and 5.1, respectively.

In order to place HD 152843 into a wider context, Fig. 9 shows the position of planet b and c in the radius-insolation diagram

alongside all known exoplanets (grey points). Multiplanet systems with measured masses around stars brighter than $V$ 10 are shown by the orange circles (see Appendix A for more detail on these systems). HD 152843 b and HD 152843 c are depicted by the blue triangle and pink square, respectively. The figure highlights a noticeable lack of well-characterized multiplanet systems around bright stars, which are key for comparative atmospheric studies. Furthermore, it shows that the planet c lies in a sparsely populated region of parameter space. This makes it valuable, as the characterization of planets in

**Table 3.** System parameters.

| Parameter | Prior[a] | Value[b] | Comments |
|---|---|---|---|
| *Model Parameters for HD 152843b* | | | |
| Orbital period $P_{orb}$ (d) | $U[11.5, 11.7]$ | $11.6264^{+0.0022}_{-0.0025}$ | |
| Transit epoch $T_0$ (BJD - 2457000) | $U[1994.25, 1994.30]$ | $1994.2831^{+0.0024}_{-0.0029}$ | |
| Parametrization $e \sin\omega$ | $U[-1, 1]$ | $-0.11^{+0.19}_{-0.28}$ | The code ensures $e < 1$ |
| Parametrization $e \cos\omega$ | $U[-1, 1]$ | $-0.07^{+0.37}_{-0.38}$ | The code ensures $e < 1$ |
| Scaled planet radius $R_p/R_*$ | $U[0, 0.1]$ | $0.02201^{+0.00081}_{-0.00073}$ | |
| Impact parameter, $b$ | $U[0, 1.1]$ | $0.32^{+0.27}_{-0.20}$ | |
| Doppler semi-amplitude, $K$ (m s$^{-1}$) | $U[0, 50]$ | $3.09^{+1.76}_{-1.66}$ | $2\sigma$ detection |
| *Model Parameters for HD 152843c* | | | |
| Orbital period $P_{orb}$ (d) | $U[19.26, 35]$ | $24.38^{+6.23}_{-3.4}$ | Truncated posterior (see Fig. 6) |
| Transit epoch $T_0$ (BJD - 2457000) | $U[2002.73, 2002.8]$ | $2002.7708^{+0.0011}_{-0.0011}$ | |
| Parametrization $e \sin\omega$ | $U[-1, 1]$ | $0.05^{+0.19}_{-0.21}$ | The code ensures $e < 1$ |
| Parametrization $e \cos\omega$ | $U[-1, 1]$ | $0.04^{+0.38}_{-0.37}$ | The code ensures $e < 1$ |
| Scaled planet radius $R_p/R_*$ | $U[0, 0.1]$ | $0.03764^{+0.00069}_{-0.00074}$ | |
| Impact parameter, $b$ | $U[0, 1.1]$ | $0.49^{+0.10}_{-0.11}$ | |
| Doppler semi-amplitude, $K$ (m s$^{-1}$) | $U[0, 50]$ | 7.1 | Upper limit (99 per cent interval of the posterior) |
| *Other Parameters* | | | |
| Stellar density $\rho_*$ (g cm$^{-3}$) | $N[0.56, 0.04]$ | $0.568^{+0.042}_{-0.043}$ | |
| Parametrized limb-darkening coefficient $q_1$ | $U[0, 1]$ | $0.183^{+0.156}_{-0.09}$ | $q_1$ parameter as in Kipping (2013) |
| Parametrized limb-darkening coefficient $q_2$ | $U[0, 1]$ | $0.47^{+0.35}_{-0.31}$ | $q_2$ parameter as in Kipping (2013) |
| Offset velocity HARPS-N (km s$^{-1}$) | $U[-0.50, 0.50]$ | $0.0007^{+0.0013}_{-0.0012}$ | |
| Offset velocity EXPRES (km s$^{-1}$) | $U[-0.50, 0.50]$ | $0.006^{+0.0021}_{-0.0021}$ | |
| Jitter HARPS-N (m s$^{-1}$) | $U[0, 100]$ | $3.02^{+1.47}_{-1.27}$ | |
| Jitter EXPRES (m s$^{-1}$) | $U[0, 100]$ | $1.06^{+1.88}_{-0.82}$ | |
| Jitter TESS (ppm) | $U[0, 500]$ | $39^{+35}_{-27}$ | |
| *Derived parameters HD 152843b* | | | |
| Planet mass ($M_\oplus$) | ... | $11.56^{+6.58}_{-6.14}$ | $2\sigma$ detection |
| Planet radius ($R_\oplus$) | ... | $3.41^{+0.14}_{-0.12}$ | |
| Planet density $\rho$ (g cm$^{-3}$) | ... | $1.58^{+0.96}_{-0.83}$ | |
| Semimajor axis $a$ (au) | ... | $0.1053^{+0.003}_{-0.0031}$ | |
| Eccentricity $e$ | ... | $0.14^{+0.25}_{-0.10}$ | Upper limit of 0.72 (99 per cent interval of the posterior) |
| Transit duration $\tau$ (h) | ... | $5.53^{+0.11}_{-0.11}$ | |
| Orbit inclination $i$ (deg) | ... | $88.85^{+0.73}_{-0.73}$ | |
| Insolation $F_p$ ($F_\oplus$) | ... | $255.7^{+21.6}_{-19.7}$ | |
| *Derived parameters HD 152843c* | | | |
| Planet mass ($M_\oplus$) | ... | 27.5 | Upper limit (99 per cent interval of the posterior) |
| Planet radius ($R_\oplus$) | ... | $5.83^{+0.14}_{-0.14}$ | |
| Planet density $\rho$ (g cm$^{-3}$) | ... | 0.82 | Upper limit (99 per cent interval of the posterior) |
| Eccentricity $e$ | ... | $0.115^{+0.173}_{-0.08}$ | Upper limit of 0.59 (99 per cent interval of the posterior) |
| Transit duration $\tau$ (h) | ... | $6.359^{+0.087}_{-0.071}$ | |
| Orbit inclination $i$ (deg) | ... | $88.89^{+0.18}_{-0.15}$ | |

[a] $U[a, b]$ refers to uniform priors between $a$ and $b$, $N[a, b]$ to Gaussian priors with mean $a$ and standard deviation $b$. [b] Inferred parameters and errors are defined as the median and 68.3 per cent credible interval of the posterior distribution.

this underpopulated region of parameters can help constrain theories of planet formation and evolution.

The two planets also stand out in terms of their bulk densities. Given the minimum radius and upper mass limit of HD 152843 c, this planet has a density < 0.82 g cm$^{-3}$, suggesting that the planet has an extended gaseous envelope. Similarly, the density of HD 152843 b

One possible explanation for the expected low density of planet c is that it formed at a greater distance from the host star prior to migrating to its current orbit. This would have allowed the planet to accrete a significant H/He envelope, due to the colder and less dense gas present farther away from the host star. Furthermore, planets that undergo this type of migration are often found to be the outer planets in mean-motion resonant chains (Lee & Chiang 2016). Future spectroscopic and photometric observations will allow us to further

is $1.58^{+0.96}_{-0.83}$ g cm$^{-3}$, making both planets prime candidates for atmospheric characterization, as discussed further in Section 5.4.

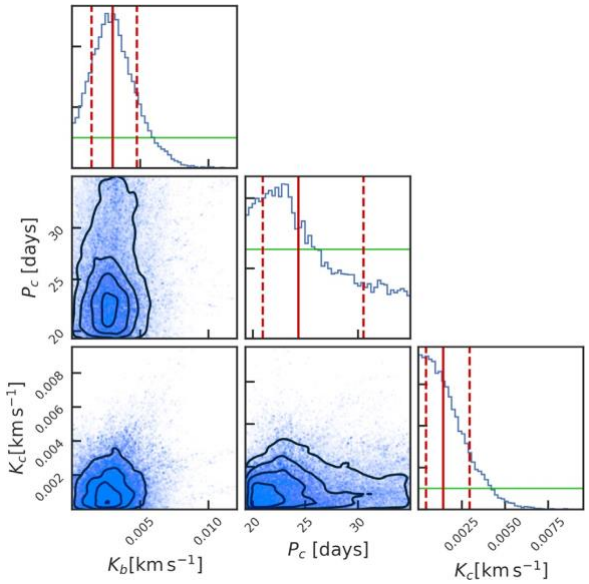


**Figure 6.** Corner plot for $K_b$, $P_c$, and $K_c$. First row in each column shows the posterior distribution (blue line) together with the prior shape (solid green line). Vertical solid (red) lines show the median, and vertical dashed (red) lines indicate 68.3 per cent credible intervals. The rest of sub-plots show the correlation between parameters.Transparent blue points show individual samples and solid black lines show iso-density contours.

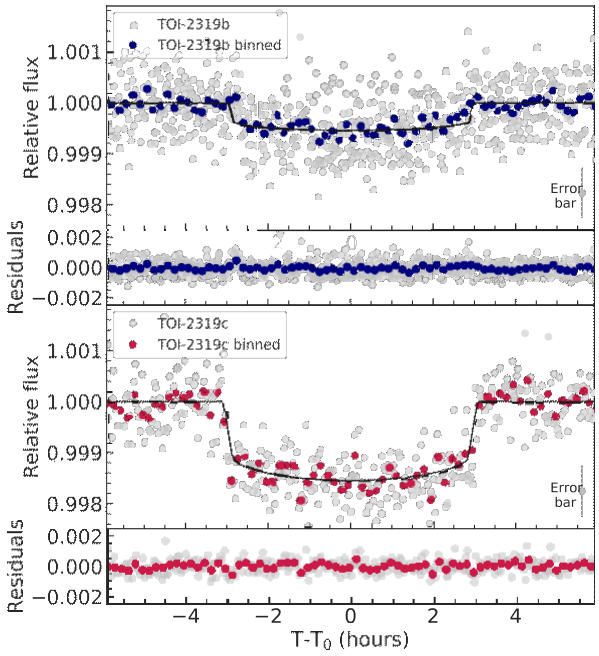


**Figure 7.** Phase-folded *TESS* light curve of HD 152843 b (upper panel) and HD 152843 c (lower panel). Nominal *TESS* data are shown in light grey together with 10-min binned data in solid colour. The inferred transit model for each planet is overplotted with a solid black line. An example of the nominal white noise in the data is also shown.

constrain the orbital period of planet c in order to determine whether the two planets are in resonance with one another.

Alternatively, the two planets could have formed in situ and their differing planet properties resulted from subsequent diverging evolutionary pathways. For example, extreme ultraviolet irradiation from the host star could have enabled atmospheric loss through photoevaporation of the inner planet (Chen & Rogers 2016; Owen & Wu 2016), stripping it of its extended gaseous envelope, while the outer planet could have been inflated, resulting in the observed low density of planet c.

Theory also suggests that the low density of the planets could be due to tidal heating, which could result in an increase in entropy (e.g. Millholland 2019) and thus an inflated radius. Finally, Gao & Zhang (2020) and Wang & Dai (2019) independently suggest that the apparent radii could be enhanced by photochemical hazes in the atmospheres, resulting in an underestimate of the densities of planets. Future transmission spectra of planet c, for example at mid-infrared wavelengths where the atmosphere is less affected by hazes, will allow us to differentiate between different formation scenarios and therefore provide useful constraints for theoretical models of planet formation and migration.

### 5.1 Transit Timing Variations prospects

Transit Timing Variations or TTVs are often observable in multi-planet systems as two planets dynamically interact, as predicted by Agol et al. (2005) and Holman & Murray (2005). This is especially the case when planets are near orbital resonance, which is potentially true for HD 152843. Measuring TTVs, especially when combined with RV data allows for the refinement of planetary mass and orbital parameters, critical for interpreting atmospheric transmission spectra in smaller planets (Batalha et al. 2019). It can also enable the detection of inclined non-transiting planets and can therefore lend insight into system demographics and architectures (Brakensiek & Ragozzine 2016).

TTVs were assessed for this system using the best-fitting planetary parameters across a range of mass, period, and eccentricity solutions using the TTV Fast framework of *n*-body simulations (Deck et al. 2014). Maximum likelihood solutions for the periods of planets b and c indicate a possible 2:1 resonance, which would result in TTVs with an amplitude ranging from 5–40 min, and a super period of approximately 2–3 yr, allowing for follow-up observations to detect discernible TTVs on the scale of about a year. This amplitude would be greatly increased for non-zero eccentricities. In the window of possible period solutions, further resonant solutions include a 5:3 resonance; however, significant TTVs would not be observed away from resonance. Follow-up studies of this system should enable us to significantly constrain planetary masses, eccentricities, and other orbital parameters, given both the presence or absence of significant TTVs.

### 5.2 Rossiter–McLaughlin effect prospects

The moderate projected rotational velocity of HD 152843 ($v \sin i$ 8.2 km s$^{-1}$) makes it a good candidate for studying the Rossiter–McLaughlin effect (RM; McLaughlin 1924; Rossiter 1924), which provides an estimate of the spin–orbit alignment of the orbiting planets with the host star (e.g. Schneider 2000). The RM effect helps to shed light on to the dynamical history of the system, as mechanisms such as planet–disc interactions help to preserve the initial spin–orbit alignment, while planet–planet interactions promote misalignment (e.g. Chatterjee et al. 2008; Deeg et al. 2009; Storch, Lai & Anderson 2017). The number of multiplanet systems with measured obliquities remains small (e.g. Dalal et al. 2019; Hjorth et al. 2021). We estimate the RM effect to be $3.71^{+0.89}_{-0.74}$ m s$^{-1}$ and $9.56^{+2.65}_{-2.7}$ m s$^{-1}$ for HD 152843 b and c, respectively (Winn 2010).

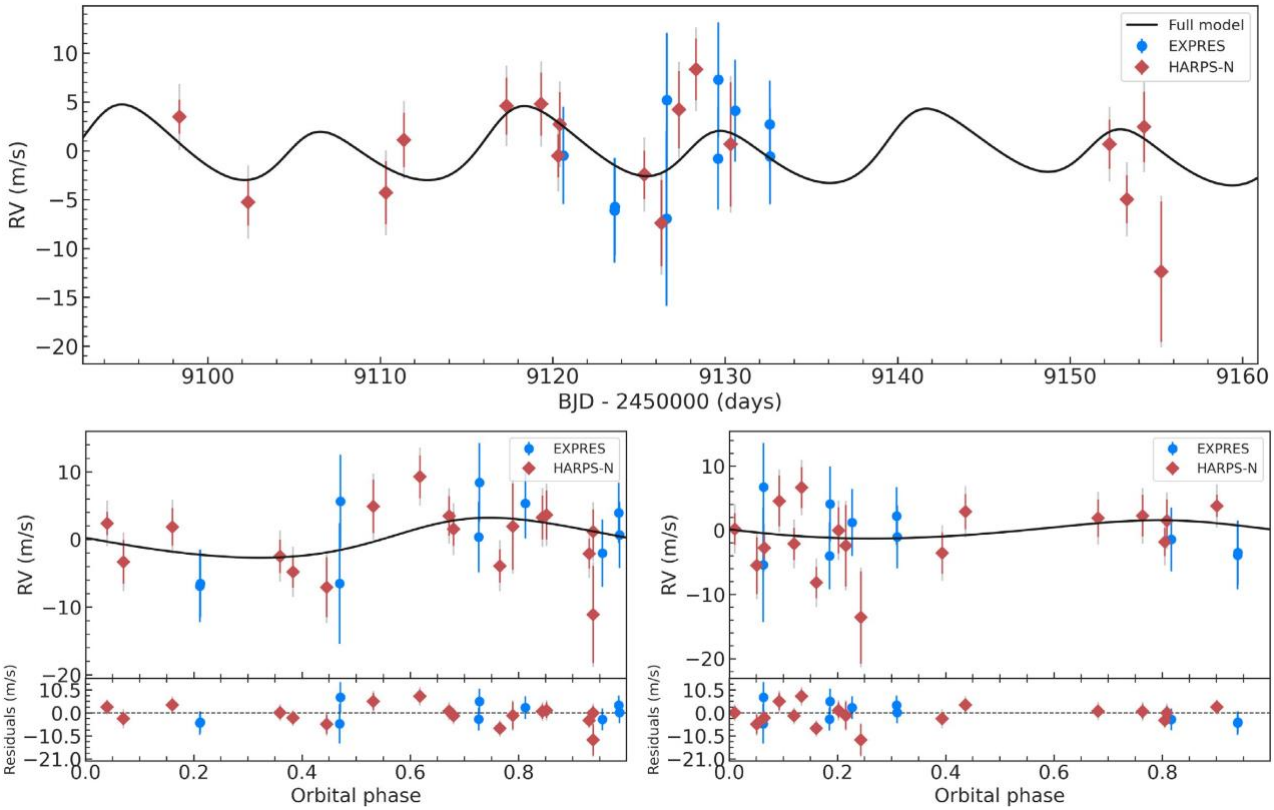


**Figure 8.** RV time-series (upper panel) and phase-folded RV plots for HD 152843 b (lower left panel) and HD 152843 c (lower right panel) following the subtraction of the instrumental offsets. HD 152843 c plot has been phase folded using a period of 24.5 d. HARPS-N (red diamonds) and EXPRES (blue circles) RV measurements along with their nominal uncertainties are shown in each panel. The vertical grey lines mark the error bars including jitter. Solid black lines show the respective inferred model.

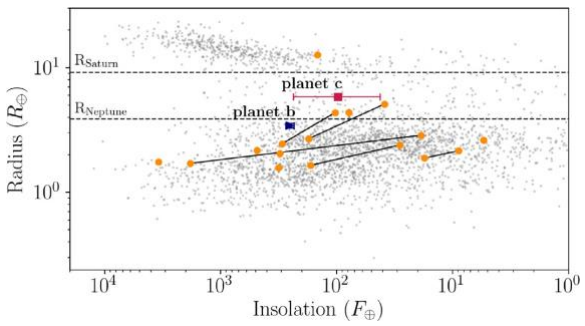


**Figure 9.** Planet insolation-radius diagram of confirmed exoplanets from the NASA Exoplanet Archive (grey points, retrieved 2021 April). Orange points show members of systems with more than one planet, with mass measurements better than 50 per cent and around stars brighter than $\lesssim 10$ (Akeson et al. 2013, see Appendix A). The black lines connect planets that are within the same system. Planets that are not connected by a black line are in multisystems where only one planet has a mass measurement with better than 50 per cent accuracy. HD 152843 b and HD 152843 c are shown by the blue triangle and pink square, respectively.

Future precision RV observations (for example, we obtained a typical precision of 4 m s$^{-1}$ for this target with HARPS-N) will be able to detect the RM of planet c, thus allowing for the determination of the true obliquity of the target.

### 5.3 Orbital dynamics

Given the uncertainty around the period of planet c, we are unable to perform a full dynamical analysis of the system, as in the work of e.g. Horner et al. (2019). However, we can estimate the system stability by comparing the possible period scenarios of planet c to the general cases presented by Agnew et al. (2019).

In general, those authors found that dynamical stability can be broken into three broad regimes: highly stable orbits (when the two orbits do not approach more closely than several mutual Hill radii; and when the two orbits are more widely spaced than the 1:2 MMR); qualified stability (when the orbits are closer together than the 1:2 resonance, but have stability ensured by mutual MMR) and likely strong instability (which typically occurs for orbits that either cross, or are located closer than the 1:2 resonance, while not benefiting from the protection of another MMR). In this light, we consider it likely that the 23 d period estimate for planet c, and any period solution longer than that, is almost certainly a feasible, stable solution – it places that planet beyond the location of the 1:2 MMR, and so is stable so long as its eccentricity is less than ~0.3 (greater than this would bring the periastron distance of planet c too close to planet b).

The minimum possible period of 19.25 d lies interior to the 1:2 resonance, and is close to the 3:5 resonance (period of 19.35 d). As can be seen in the fourth row of fig. 4 in Agnew et al. (2019), this region is still likely to be stable, so long as the orbital eccentricity for planet c is below ~0.2.

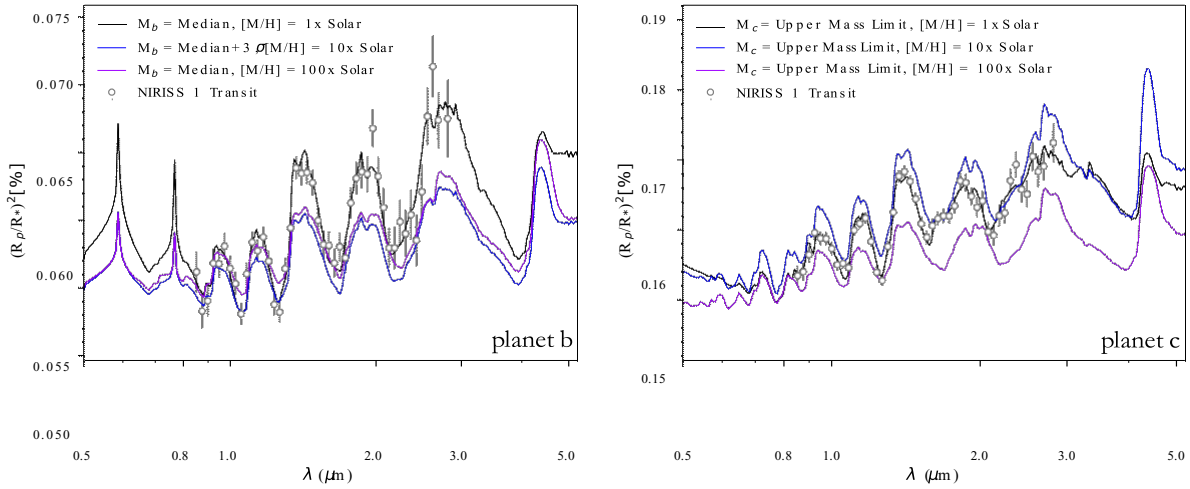


**Figure 10.** Models generated for planets b and c in the left-hand and right-hand panels, respectively. Each panel shows three models describing plausible atmospheric scenarios. In black, we present an atmospheric model which has a metallicity of 1× solar, considering the RV extracted median mass and upper mass limit for planets b and c, respectively. In purple, we present an atmospheric model which has a metallicity of 100× solar considering the RV extracted median mass and upper mass limit for planets b and c, respectively. In blue, we present an atmospheric model which has a metallicity of 10 solar, however, we consider the RV extracted median mass plus the 3$\sigma$ upper uncertainty for planet b and the upper mass limit for planet c. We overplot the simulated JWST NIRISS/SOSS observations for the 1× solar case to emphasize the precision we would obtain from a single transit observation.

### 5.4 Feasibility of atmospheric characterization

Known transiting multiplanetary systems with measured masses, around stars bright enough for atmospheric follow-up i.e. brighter than $V = 10$, are exceedingly rare. The brightness of HD 152843 ($V$ 8.855), combined with the large radii of the planets, as shownin Fig. 9, make them key targets for atmospheric characterization via transmission spectroscopy. We assess the feasibility of suchan observation using the transmission spectroscopy metric (TSM; Kempton et al. 2018), which provides the estimated SNR of a 10 h observation with JWST/NIRISS (Doyon et al. 2012), if a cloud-free atmosphere is assumed. Based on planetary masses of 11.58 and 27.5 $M_\oplus$ (Table 3), and assuming a mean molecular weightof 2.3, we find the TSM to be 65 and 103, for HD 152843 b and HD 152843 c, respectively. The latter compares well with several of the targets currently included in JWST ERS and GTO programs, and is better than the cut-off thresholds for follow-up observations, of 96, as suggested by Kempton et al. (2018). The TSM of 103 places planet c at least among the top 50 per cent of candidates suitable for atmospheric characterization as outlined by Kempton et al. (2018). Furthermore, as the planet mass used to determine this value is an upper mass limit, the TSM of planet c is likely to be significantly higher, likely placing it amongst the top 25 per cent of candidates best suited for atmospheric characterization.

### 5.5 Atmospheric modelling

To assess the possibility of differentiating between different atmospheric scenarios, we generated an array of forward models using the open source code CHIMERA (Line et al. 2013) and compared these to synthetic observations of each planet which were generated using PANDEXO (Batalha et al. 2017) for 1 transit observation using JWST NIRISS/SOSS. A subset of these models can be seen in Fig. 10. For each planet, we modelled a cloud free atmosphere with an isothermal temperature profile set to the derived temperature from Table 1. For have a solar C/O ratio and metallicities of 1 , 10 , and 100 solar, respectively. We used the chemical grid developed by Kreidberg et al. (2015). In Fig. 10, we highlight a subset of the models. We do not show the models for scenario 3 because the lower masses would have larger observable features than the median and hence would be easier to observe. For each planet, we present three models: in black we show the model for the mass and 1 solar metallicity, in purple we show the model for the mass and 100 solar and finally in blue we show the model for the mass 3 and 10 metallicity. We use the mean mass and upper mass limits for planets b and c, respectively. We then overplot the predictive observations obtained from JWST NIRISS/SOSS generated using the 1 solar median mass models. The left-hand panel, corresponding to planet b, shows that while with a single transit it is possible to detect the atmosphere, there remains a degeneracy between the metallicity and the mass of the planet. Future RV follow-up observations will enable us to break this degeneracy. The right-hand panel, corresponding to planet c, shows that the simulated data have extremely small error bars, due to the bright star and long transit duration. These small error bars allow us to break the degeneracy between planetary mass and atmospheric metallicity. These simulations emphasize how promising these targets are for follow-up measurements and atmospheric characterization.

## 6 SUMMARY AND CONCLUSIONS

We present the discovery of a multiplanet system (HD 152843, TIC 349488688, TOI 2319) with a Neptune and a sub-Saturn sized planet, observed in Sector 25 of the nominal *TESS* mission. The *TESS* light curve yields two transit events for the inner planet ($P_b = 11.6264^{+0.0022}_{-0.0025}$ d) and a single transit event for the outer planet ($P_c = 19.26$–35 d). All three transit events were identified

planet c, we modelled the upper mass limit of 27.5 $M_\oplus$ and for planet b we considered three mass scenarios: (1) the median mass, (2) the median mass the 3$\sigma$ uncertainty, and (3) the median mass – the 3$\sigma$ uncertainty. We did this so that we could capture the full range of possible transmission spectra. We then modelled the atmospheres to

by volunteers taking part in the PHT citizen science project (Eisner et al. 2021), and the events vetted for instrumental and astrophysical false positives using the LATTE vetting suite (Eisner et al. 2020b). Furthermore, we statistically validated both planets using the open source software VESPA (Morton 2012, 2015; Morton et al. 2016) by taking into consideration the decrease in FPP given the multiplicity of system (Lissauer et al. 2011, 2012, 2014).

Additionally, we obtained ground-based spectroscopic follow-up observations with HARPS-N and EXPRES in order to both constrain

the orbit and planet parameters as well as to refine the stellar properties. Joint modelling of the light curve and RVs allowed us to constrain the mass of the inner planet to $M_b$ $11.56^{+6.58}_{-6.14}$ $M_\oplus$ ($2\sigma$ detection) and obtain an upper mass limit for the outer planet of $M_c < 27.5$ $M_\oplus$. Furthermore, we constrained the orbit of the outer, singly transiting planet, to be between 19.26 and 35, with the truncated model posteriors slightly favouring a period of around 23 d. This suggests the possibility of a 2:1 resonance with the innermost planet.

Following this, we discuss the implications of a resonance between the two planets in terms of the TTVs and show that a 2:1 resonance would result in TTVs with an amplitude between 5 and 40 min. We also show that the planets are suitable targets for measuring the spin–orbit alignment of the system via the RM effect, with expected amplitudes of $3.71^{+0.89}_{-0.74}$ m s$^{-1}$ and $9.56^{+2.65}_{-2.7}$ m s$^{-1}$ for HD 152843 b and c, respectively.

We also show that the properties of HD 152843 c, which likely has an extended H/He atmosphere, combined with the brightness of the host star make it a promising targets for atmospheric characterization. We use the TSM (Kempton et al. 2018) to show that with a 10 h observation with JWST/NIRISS, we would obtain an SNR of 103. As an upper mass limit was used in this calculation, the value is likely to be significantly higher, making it a prime target for future atmospheric characterization.

Finally, we generate forward models of different atmospheric compositions and compare these to synthetic observations for each planet in order to differentiate between different atmospheric scenarios. With this we show that with a single JWST NIRISS/SOSS we would be able to detect the atmospheres of these planets. Furthermore, the brightness of the star combined with the transit duration of planet c results in small uncertainties in the simulated spectra, which allow us to break the degeneracy between planetary mass and atmospheric metallicity for the outer planet. Future RV follow-up observations will allow us to also break this degeneracy for planet b.

Overall, we show that this is a very promising target for future ground and space-based follow-up observations. Continued future efforts with HARPS-N and EXPRES will be able to conclusively determine the masses of both planets and the orbital period of planet c, as well as search for the RM effect. Additionally, ground-based photometers, such as LCO/Sinistro (Brown et al. 2013), will allow us to observe future transit events and constrain possible TTVs, as will the space-based missions such as CHEOPS (Broeg et al. 2013), or the upcoming PLATO mission (Rauer et al. 2014). HD 152843 is also scheduled to be re-observed by the *TESS* mission during Sector 52 (2022 May–June). Finally, observations with JWST or ARIEL (Tinetti et al. 2016) will help to characterize the atmospheres of these scientifically valuable planets.

## ACKNOWLEDGEMENTS

We thank all of the volunteers who participated in the Planet Hunters TESS project, as without them this work would not have been possible. We also thank the editor and the referee for their comments, which improved and clarified the manuscript. Furthermore, we are very grateful to the Director of the TNG for allocating time for the HARPS-N observations from the directors discretionary time through the program ID A41DDT4.

NE also thanks the LSSTC Data Science Fellowship Program, which is funded by LSSTC, NSF Cybertraining Grant no. 1829740, the Brinson Foundation, and the Moore Foundation; her participation in the program has benefited this work. AM acknowledges support from the senior Kavli Institute Fellowships. JT is a Penrose Graduate Scholar and would like to thank the Oxford Physics Endowment for Graduates (OXPEG) for funding this research. Furthermore, NE, NZ, BN, and SA acknowledge support from the UK Science and Technology Facilities Council (STFC) under grant codes ST/R505006/1, ST/S505638/1 and consolidated grant no. ST/S000488. This work also received funding from the European Research Council (ERC) under the European Union's Horizon 2020 research and innovation program (Grant agreement no. 865624).

This paper includes data collected by the *TESS* spacecraft, and we are grateful to the entire *TESS* team in obtaining and providing the light curves used in this analysis. Funding for the *TESS* mission is provided by the NASA Science Mission Directorate. We obtained the publicly released *TESS* data from the Mikulski Archive for Space Telescopes (MAST). Resources supporting this work were also provided by the NASA High-End Computing (HEC) Program through the NASA Advanced Supercomputing (NAS) Division at Ames Research Center for the production of the SPOC data products. Furthermore, these results also made use of the Lowell Discovery Telescope at Lowell Observatory. Lowell is a private, non-profit institution dedicated to astrophysical research and public appreciation of astronomy and operates the LDT in partnership with Boston University, the University of Maryland, the University of Toledo, Northern Arizona University and Yale University. This work used the EXtreme PREcision Spectrograph (EXPRES) that was designed and commissioned at Yale with financial support by the U.S. National Science Foundation under MRI-1429365 and ATI-1509436 (PI D. Fischer). Finally, the research leading to these results has partially received funding from the KU Leuven Research Council (grant C16/18/005: PARADISE), from the Research Foundation Flanders (FWO) under grant agreement G0H5416N (ERC Runner Up Project), as well as from the BELgian federal Science Policy Office (BELSPO) through PRODEX grant PLATO.

Finally, NE and OB wish to thank the Asterix comics, which provided the inspiration for our in-house nickname for this planet system of *Idefix*.

This research made use of Astropy, a community-developedcore Python package for Astronomy (Astropy Collaboration 2013), MATPLOTLIB (Hunter 2007), PANDAS (McKinney et al. 2010), NUMPY (Walt, Colbert & Varoquaux 2011), ASTROQUERY (Ginsburg et al. 2019), and SKLEARN (Pedregosa et al. 2011).

## DATA AVAILABILITY

The *TESS* data used within this article are hosted and made publicly available by the Mikulski Archive for Space Telescopes (MAST; http://archive.stsci.edu/tess/). Similarly, the Planet Hunters TESS classifications made by the citizen scientists can be found on the Planet Hunters Analysis Database (PHAD; https://mast.stsci.edu/phad/), which is also hosted by MAST. The two planet candidates and their properties have been uploaded to the Exoplanet Follow-up Observing Program for TESS (ExoFOP-TESS) website as community TOIs (cTOIs; https://exofop.ipac.caltech.edu/tess/target.php?id = 349488688).

The models of the transit events and the data validation report used for the vetting of the target were both generated using publicly available open software codes, PYANETI and LATTE.

## REFERENCES

Agnew M. T., Maddison S. T., Horner J., Kane S. R., 2019, MNRAS, 485, 4703
Agol E., Steffen J., Sari R., Clarkson W., 2005, MNRAS, 359, 567
Aigrain S., Irwin M., 2004, MNRAS, 350, 331

Akeson R. L. et al., 2013, PASP, 125, 989
Anglada-Escude´ G., Butler R. P., 2012, ApJS, 200, 15
Astropy Collaboration, 2013, A&A, 558, A33
Bailer-Jones C. A. L., Rybizki J., Fouesneau M., Mantelet G., Andrae R., 2018, AJ, 156, 58
Baranne A. et al., 1996, A&AS, 119, 373
Barragán O., Gandolfi D., Antoniciello G., 2019, MNRAS, 482, 1017
Barros S. C. C. et al., 2017, A&A, 608, A25
Batalha N. E. et al., 2017, PASP, 129, 064501
Batalha N. E., Lewis T., Fortney J. J., Batalha N. M., Kempton E., Lewis N. K., Line M. R., 2019, ApJ, 885, L25
Blackman R. T. et al., 2020, AJ, 159, 238
Borucki W. J., Koch D., Kepler Science Team, 2010, AAS/Division for Planetary Sciences Meeting Abstracts, Vol. 42, p. 47.03
Brakensiek J., Ragozzine D., 2016, ApJ, 821, 47
Broeg C. et al., 2013, in Saglia R., ed., EPJ Web Conf., Hot Planets and Cool Stars. 47, p. 03005
Brown T. M. et al., 2013, PASP, 125, 1031
Bruntt H. et al., 2010, MNRAS, 405, 1907
Buchhave L. A. et al., 2012, Nature, 486, 375
Buchhave L. A. et al., 2014, Nature, 509, 593
Carleo I. et al., 2020, AJ, 160, 114
Chatterjee S., Ford E. B., Matsumura S., Rasio F. A., 2008, ApJ, 686, 580
Chen H., Rogers L. A., 2016, ApJ, 831, 180
Choi J., Dotter A., Conroy C., Cantiello M., Paxton B., Johnson B. D., 2016, ApJ, 823, 102
Christiansen J. L. et al., 2017, AJ, 154, 122
Claret A., 2017, A&A, 600, A30
Cosentino R. et al., 2012, in McLean I. S., Ramsay S. K., Takami H., eds, Proc. SPIE Conf. Ser. Vol. 8446, Ground-Based and Airborne Instrumentation for Astronomy IV. SPIE, Bellingham, p. 84461V
Cosentino R. et al., 2014, in Ramsay S. K., McLean I. S., Takami H., eds, Proc. SPIE Conf. Ser. Vol. 9147, Ground-Based and Airborne Instrumentation for Astronomy V. SPIE, Bellingham, p. 91478C
Crossfield I. J. M. et al., 2016, ApJS, 226, 7
Cutri R. M. et al., 2003, VizieR Online Data Catalog, II/246
Cutri R. M. et al., 2013, VizieR Online Data Catalog, II/328
Dalal S., Hebrard G., Lecavelier Des Etangs A., Petit A., Bourrier V., Laskar J., Konig P.-C., Correia A. C. M., 2019, AAS/Division for Extreme Solar Systems Abstracts. p. 202.04
Deck K. M., Agol E., Holman M. J., Nesvorný D., 2014, ApJ, 787, 132
Deeg H. J. et al., 2009, A&A, 506, 343
Dietrich J., Apai D., 2020, AJ, 160, 107
Doyon R. et al., 2012, in Mark C. C., Giovanni G. F., Howard A. M., Jacobus M. O., Jr., eds, Proc. SPIE Conf. Ser. Vol. 8442, Space Telescopes and Instrumentation 2012: Optical, Infrared, and Millimeter Wave. SPIE, Bellingham, p. 84422R
Dragomir D. et al., 2019, ApJ, 875, L7
Dressing C. D. et al., 2015, ApJ, 800, 135
Eisner N. L. et al., 2021, MNRAS, 501, 4669
Eisner N., Lintott C., Aigrain S., 2020a, J. Open Source Softw., 5, 2101
Eisner N. L. et al., 2020b, MNRAS, 494, 750
Espinoza N. et al., 2020, MNRAS, 491, 2982
Feroz F., Hobson M. P., Cameron E., Pettitt A. N., 2019, Open J. Astrophys., 2, 10
Findeisen K., Hillenbrand L., Soderblom D., 2011, AJ, 142, 23
Fischer D. A. et al., 2012, MNRAS, 419, 2900
Fortenbach C. D., Dressing C. D., 2020, PASP, 132, 054501
Fridlund M. et al., 2020, MNRAS, 498, 4503
Gaia Collaboration, 2021, A&A, 649, A1
Gaia Collaboration, 2018, A&A, 616, A1
Gandolfi D. et al., 2019, ApJ, 876, L24
Gao P., Zhang X., 2020, ApJ, 890, 93
Gilbert E. A. et al., 2020, AJ, 160, 116
Ginsburg A. et al., 2019, AJ, 157, 98
Girardi L., Groenewegen M. A. T., Hatziminaoglou E., da Costa L., 2005, A&A, 436, 895
Hjorth M., Albrecht S., Hirano T., Winn J. N., Dawson R. I., Zanazzi J. J., Knudstrup E., Sato B., 2021, Proc. Natl. Acad. Sci., 118, 2017418118
Holman M. J., Murray N. W., 2005, Science, 307, 1288
Horner J. et al., 2019, AJ, 158, 100
Huang C. X. et al., 2018, ApJ, 868, L39
Hunter J. D., 2007, Comput. Sci. Eng., 9, 90
Høg E. et al., 2000, A&A, 355, L27
Jenkins J. M. et al., 2016, in Chiozzi G., Guzman J. C., eds, Proc. SPIE Conf. Ser. Vol. 9913, Software and Cyberinfrastructure for Astronomy IV. SPIE, Bellingham, p. 99133E
Jurgenson C., Fischer D., McCracken T., Sawyer D., Szymkowiak A., Davis A., Muller G., Santoro F., 2016, in Evans C. J., Simard L., Takami H., eds, Proc. SPIE Conf. Ser. Vol. 9908, Ground-Based and Airborne Instrumentation for Astronomy VI. SPIE, Bellingham, p. 99086T
Kempton E. M. R. et al., 2018, PASP, 130, 114401
Kipping D. M., 2013, MNRAS, 435, 2152
Kovács G., Zucker S., Mazeh T., 2002, A&A, 391, 369
Kreidberg L., 2015, PASP, 127, 1161
Kreidberg L. et al., 2015, ApJ, 814, 66
Kurucz R.-L., 2013, Astrophysics Source Code Library, record ascl:1303.024
Latham D. W. et al., 2011, ApJ, 732, L24
Lee E. J., Chiang E., 2016, ApJ, 817, 90
Leleu A. et al., 2021, A&A, 649, A26
Levine S. E. et al., 2012, in Proc. SPIE, 2012, vol. 8444, p. 844419
Lienhard F. et al., 2020, MNRAS, 497, 3790
Line M. R. et al., 2013, ApJ, 775, 137
Lintott C. J. et al., 2008, MNRAS, 389, 1179
Lintott C. et al., 2011, MNRAS, 410, 166
Lissauer J. J. et al., 2011, ApJS, 197, 8
Lissauer J. J. et al., 2012, ApJ, 750, 112
Lissauer J. J. et al., 2014, ApJ, 784, 44
McKinney W. et al., 2010, in van der Walt S., Millman J., eds, Proc. 9th Python Sci. Conf. (SciPy), Data Structures for Statistical Computing in Python. Austin, Texas, p. 51
McLaughlin D. B., 1924, ApJ, 60, 22
Mamajek E. E., Hillenbrand L. A., 2008, ApJ, 687, 1264
Mandel K., Agol E., 2002, ApJ, 580, L171
Mann A. W. et al., 2020, AJ, 160, 179
Millholland S., 2019, ApJ, 886, 72
Mortier A., Sousa S. G., Adibekyan V. Z., Brandão I. M., Santos N. C., 2014, A&A, 572, A95
Mortier A. et al., 2020, MNRAS, 499, 5004
Morton T. D., 2012, ApJ, 761, 6
Morton T. D., 2015, Astrophysics Source Code Library, record ascl:1503.011
Morton T. D., Bryson S. T., Coughlin J. L., Rowe J. F., Ravichandran G., Petigura E. A., Haas M. R., Batalha N. M., 2016, ApJ, 822, 86
Noyes R. W., Hartmann L. W., Baliunas S. L., Duncan D. K., Vaughan A. H., 1984, ApJ, 279, 763
Osborn H. P. et al., 2016, MNRAS, 457, 2273
Owen J. E., Wu Y., 2016, ApJ, 817, 107
Pearson K. A., Palafox L., Griffith C. A., 2018, MNRAS, 474, 478
Pedregosa F. et al., 2011, J. Mach. Learn. Res., 12, 2825
Petersburg R. R. et al., 2020, AJ, 159, 187
Queloz D. et al., 2010, A&A, 517, L1
Quinn S. N. et al., 2019, AJ, 158, 177
Rauer H. et al., 2014, Exp. Astron., 38, 249
Ricker G. R. et al., 2015, J. Astron. Telesc. Instrum. Syst., 1, 014003
Rossiter R. A., 1924, ApJ, 60, 15
Schlegel D. J., Finkbeiner D. P., Davis M., 1998, ApJ, 500, 525
Schneider J., 2000, in Griffith C. A., Marley M. S., eds, ASP Conf. Ser. Vol. 212, From Giant Planets to Cool Stars. Astron. Soc. Pac., San Francisco, p. 284
Shulyak D., Tsymbal V., Ryabchikova T., Stütz C., Weiss W. W., 2004, A&A, 428, 993
Sneden C. A., 1973, PhD thesis, The University of Texas at Austin

Sousa S. G., 2014, in Niemczura E., Smalley B., Pych W., eds, ARES + MOOG: A Practical Overview of an Equivalent Width (EW) Method to Derive Stellar Parameters. Springer International Publishing, Switzerland, p. 297
Sousa S. G., Santos N. C., Adibekyan V., Delgado-Mena E., Israelian G., 2015, A&A, 577, A67
Stassun K. G., Torres G., 2016, AJ, 152, 180
Stassun K. G., Torres G., 2018, ApJ, 862, 61
Stassun K. G., Collins K. A., Gaudi B. S., 2017, AJ, 153, 136
Stassun K. G., Corsaro E., Pepper J. A., Gaudi B. S., 2018, AJ, 155, 22
Stassun K. G. et al., 2019, AJ, 158, 138
Storch N. I., Lai D., Anderson K. R., 2017, MNRAS, 465, 3927
Teske J. et al., 2020, AJ, 160, 96
Tinetti G. et al., 2016, in MacEwen H. A., Fazio G. G., Lystrup M., Batalha N., Siegler N., Tong E. C., eds, Proc. SPIE Conf. Ser. Vol. 9904, Space Telescopes and Instrumentation 2016: Optical, Infrared, and Millimeter Wave. SPIE, Bellingham, p. 99041X
Tkachenko A., 2015, A&A, 581, A129
Torres G., Andersen J., Giménez A., 2010, A&AR, 18, 67
Tremaine S., Dong S., 2012, AJ, 143, 94
Trifonov T., Rybizki J., Kürster M., 2019, A&A, 622, L7
Vanderburg A. et al., 2019, ApJ, 881, L19
Walt S. v. d., Colbert S. C., Varoquaux G., 2011, Comput. Sci. Eng., 13, 22
Wang L., Dai F., 2019, ApJ, 873, L1
Winn J. N., 2010, Exoplanet Transits and Occultations. University of Arizona Press, Tucson, p. 55
Yee S. W. et al., 2018, AJ, 155, 255
Zucker S., Giryes R., 2018, AJ, 155, 147

## APPENDIX A: CONFIRMED MULTIPLANET SYSTEMS

**Table A1.** Bright multiplanet system.

| Host name | Planet letter | $R_{pl}$ ($R_\oplus$) | $M_{pl}$ ($M_\oplus$) | $P_{pl}$ (d) | Vmag | No. confirmed planets | Reference |
|---|---|---|---|---|---|---|---|
| GJ 143 | b | $2.61^{0.17}_{0.06}$ | $22.7^{2.2}_{2.2}$ | $35.61253^{0.0006}_{-0.00062}$ | 8.08 | 2 | Dragomir et al. (2019) |
| HAT-P-11 | b | $4.36_{-0.06}$ | $26.698_{-2.22}$ | 4.8878 | 9.46 | 2 | Yee et al. (2018) |
| HD 106315 | b | $2.44^{0.17}_{-0.17}$ | $12.6^{3.2}_{-3.2}$ | $9.55237^{0.00089}_{-0.00089}$ | 8.951 | 2 | Barros et al. (2017) |
| | c | $4.35^{0.23}_{-0.23}$ | $15.2^{3.7}_{-3.7}$ | $21.05704^{0.00046}_{-0.00046}$ | | | |
| HD 15337 | b | $1.64^{0.06}_{-0.06}$ | $7.51^{1.09}_{-1.01}$ | $4.75615^{0.00017}_{-0.00017}$ | 9.1 | 2 | Gandolfi et al. (2019) |
| | c | $2.39^{0.12}_{-0.12}$ | $8.11^{1.82}_{-1.69}$ | $17.1784^{0.0016}_{-0.0016}$ | | | |
| HD 213885 | b | $1.745^{0.05}_{-0.05}$ | $8.83^{0.66}_{-0.65}$ | $1.00804^{0.00002}_{-0.00002}$ | 7.95 | 2 | Espinoza et al. (2020) |
| HD 23472 | b | $1.872^{1.32}_{-1.32}$ | $17.92^{1.41}_{-14.0}$ | $17.667^{0.142}_{-0.095}$ | 9.73 | 2 | Trifonov, Rybizki & Kürster (2019) |
| | c | $2.149^{0.34}_{-0.34}$ | $17.18^{1.07}_{-13.77}$ | $29.625^{0.224}_{-0.171}$ | | | |
| HD 3167 | b | $1.70^{0.08}_{-0.08}$ | $5.02^{0.38}_{-0.38}$ | $0.95962^{0.00003}_{-0.00003}$ | 8.97 | 3 | Christiansen et al. (2017) |
| | c | $2.86^{0.22}_{-0.22}$ | $9.81^{1.3}_{-1.24}$ | $29.83832^{0.0029}_{-0.0032}$ | | | |
| HD 39091 | c | $2.042^{0.05}_{-0.05}$ | $4.82^{0.84}_{-0.86}$ | $6.2679^{0.00046}_{-0.00046}$ | 5.65 | 2 | Huang et al. (2018) |
| HD 86226 | c | $2.160^{0.08}_{-0.08}$ | $7.25^{1.19}_{-1.12}$ | $3.98442^{0.00018}_{-0.00018}$ | 7.93 | 2 | Teske et al. (2020) |
| Kepler-93 | b | $1.569^{0.11}_{-0.11}$ | $4.544^{0.85}_{-0.85}$ | $4.72674^{0.000001}_{-0.000001}$ | 9.996 | 2 | Dressing et al. (2015) |
| TOI-421 | b | $2.68^{0.19}_{-0.18}$ | $7.17^{0.66}_{-0.66}$ | $5.19672^{0.00049}_{-0.00049}$ | 9.931 | 2 | Carleo et al. (2020) |
| | c | $5.09^{0.16}_{-0.15}$ | $16.42^{1.06}_{-1.04}$ | $16.06819^{0.00035}_{-0.00035}$ | | | |
| WASP-8 | b | $12.666^{0.56}_{-0.56}$ | $807.288^{104.88}_{-104.88}$ | $8.15872^{0.00001}_{-0.00001}$ | 9.789 | 2 | Queloz et al. (2010) |

*Note.* Confirmed exoplanets from the NASA Exoplanet Archive that are members of systems with more than one planet, with mass measurements better than 50 per cent and around stars brighter than $V = 10$ (Akeson et al. 2013). All parameters are as listed in the NASA Exoplanet Archive as of 2021 April.

This paper has been typeset from a TEX/LATEX file prepared by the author.